ACS OMEGA

Open Access

http://pubs.acs.org/journal/acsodf

Article

Influence of Zinc Substitution on the Structural, Dielectric, and Gas-Sensing Properties of $Mg_{1-x}Zn_xFe_2O_4$ Nanoparticles

Iqra Nazir, Farhan Javaid,* Mutawara Mahmood Baig, Muhammad Shoaib Butt, and Iftikhar Hussain Gul

Cite This: *ACS Omega* 2023, 8, 34760−34767

Read Online

ACCESS | Metrics & More | Article Recommendations

ABSTRACT: In the present work, $Mg_{1-x}Zn_xFe_2O_4$ (MZFO) nanoparticles with x = 0.0, 0.2, 0.35, and 0.5 were synthesized via a chemical coprecipitation method. The study aimed to explore the effect of substituting Mg with Zn in MZFO on its structural, dielectric, and gas-sensing properties. The spinel phase formation was confirmed using X-ray diffraction, and the morphology of the prepared nanoparticles was revealed using scanning electron microscopy. Fourier transform infrared spectroscopy (FTIR) analysis confirmed the band ranges of 500−600 cm^{-1} for tetrahedral and 390−450 cm^{-1} for octahedral lattice sites. The dielectric data showed that Zn substitution in MZFO decreased both the dielectric constant and loss with increasing frequencies and attained a stagnant value at higher frequencies. Furthermore, the gas-sensing characteristics of Zn-substituted spinel ferrites at room temperature for CO_2, O_2, and N_2 were studied. The nanostructured MZFO exhibited high sensitivity in the order of $CO_2 > O_2 \gg N_2$ and showed a good response time of (∼1 min) for CO_2, demonstrating that MZFO can be a good potential candidate for gas-sensing applications.

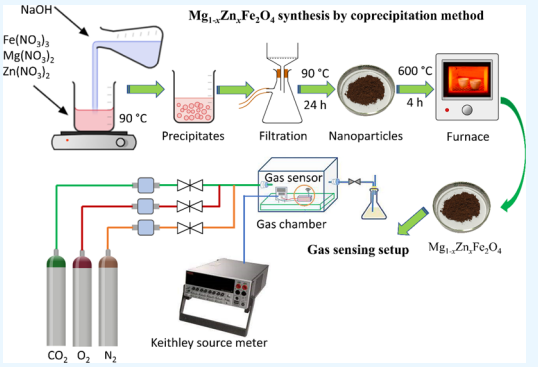

1. INTRODUCTION

Spinel ferrites (SFs) are chemical compounds substituted by transition metals and procured as powdered materials containing ferrimagnetic iron oxides. They have unique structural and dielectric properties with respect to their bulk material, which is chemically and thermally stable. However, the high resistivity of ferrite nanoparticles greatly influences their dielectric and gas-sensing behavior.[1−4]

In recent times, ferrite nanoparticles have received great interest in various applications, for example, mineral separation, drug delivery systems, and cancer therapy. Furthermore, ferrite gas sensors have been developed to detect gas pollutants in the environment, automobile drains, and biological exposures.[5−7] With an increasing human population and industrial waste, detecting gases for controlling these industrial and vehicle-hazards wastes is urgently needed. The gas-sensing ability of the materials is determined by their microstructural properties, which are determined by their preparation technique. SFs are effective gas-sensing materials, and most of them exhibit remarkable selectivity toward numerous gases. Depending on the composition and route conditions, such as atmosphere and sintering temperature, the lattice site occupancy deviates, leading to a change in dielectric and optical properties.[8−10] Therefore, in ferrite engineering, both composition and process conditions are critical to attaining the required quality.

A systematic investigation of the gas-sensing properties of spinel ferrites with doping concentrations at room temperature has not been thoroughly studied yet. The key factors that affect the development of ferrite gas sensors include crystallite size, particle size, dopants, surface-to-volume ratio, sensitivity, operating temperature, and response time. As the interaction between gas and sample mainly occurs at the surface of nanoparticles, the large surface-to-volume ratio significantly increases the gas sensitivity.[11,12] The reducing gases are detected by the change in the electric conductivity of the metal oxide surface because of a chemical reaction among the gas molecules and adsorbed oxygen.

Spinel-type oxide semiconductors have been reported to be sensitive materials to gases in the air. Hankare et al.[13] confirmed that $MgFe_2O_4$ possessed gas-sensing properties for various gases. The development of new materials as gas sensors is receiving a lot of interest at present. Lower temperature materials synthesis has numerous advantages, particularly when the materials are intended to be used as gas sensors. The

Received: May 29, 2023
Accepted: July 7, 2023
Published: September 14, 2023

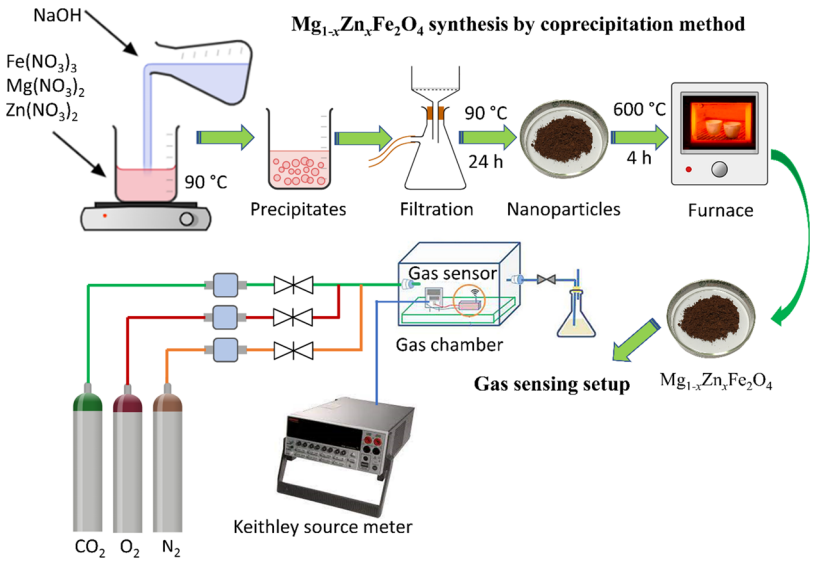

Figure 1. Schematic diagram of the experimental setup.

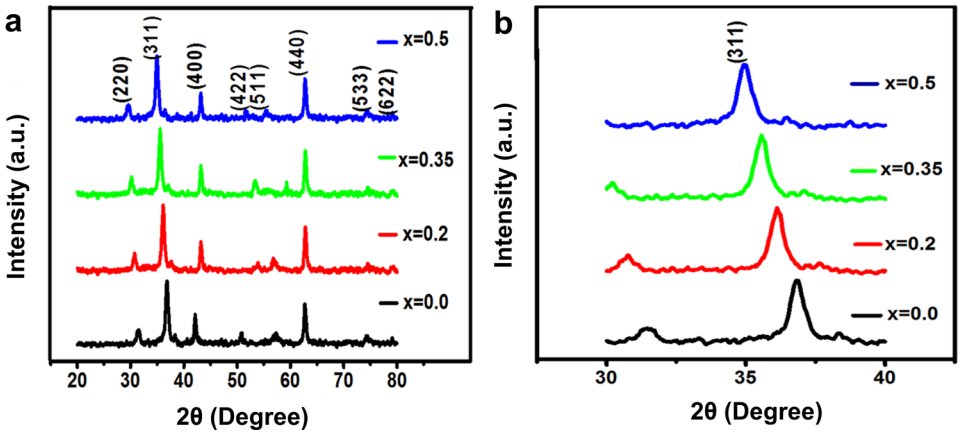

Figure 2. (a) Indexed XRD patterns correspond to all diffraction planes. (b) Indexed XRD patterns correspond to most intense peak (311) of $Mg_{1-x}ZnxFe_2O_4$ (x = 0.0, 0.2, 0.35, and 0.5) samples.

reducing gases are sensed by changes in conductivity that result from chemical reactions between the gas molecules and oxygen adsorbed on the metal oxide surface. As sensing occurs primarily on the surface of materials, the morphology of the surface has a significant influence on solid-state sensors' sensitivity. In this work, a systematic study that includes a comprehensive investigation of the physical chemistry of the synthesized nanoparticles ($Mg_{1-x}Zn_xFe_2O_4$) as well as their correlation with electrical and structural properties has been discussed. Furthermore, complex electric and impedance models were used to study the relations between dielectric properties and microstructure. As demonstrated in this study, semiconductor gas sensors have several advantages over other detection systems due to their low cost, ease of implementation, and high reliability.

2. MATERIALS AND METHODS

2.1. Synthesis of $Mg_{1-x}Zn_xFe_2O_4$ Nanoparticles. The $Mg_{1-x}Zn_xFe_2O_4$ (MZFO) nanoparticles were synthesized via the coprecipitation method. In brief, salts of $Fe(NO_3)_3{\cdot}9H_2O$, $Mg(NO_3)_2{\cdot}6H_2O$, and $Zn(NO_3)_2{\cdot}6H_2O$ purchased from EMSURE Merck, Germany (99% purity), were dissolved in deionized water (DI) in an appropriate proportion and stirred for 30 min. The NaOH solution was then added to the ferrite salt solution, followed by heating at 90 °C. The solution was then allowed to cool to room temperature. The precipitates were filtered and washed repeatedly with DI water, followed by drying at 90 °C for 24 h. The dried material under investigation was finely ground into a fine powder to attain homogeneity. The samples were then calcined at 600 °C for 4 h to obtain a well-defined spinel phase. The whole procedure was repeated for different MZFO sample compositions.

2.2. Characterization Techniques. The crystal structure and spinel phase identification were recognized via X-ray diffraction using Cu Kα radiation with a scan rate of ∼2°/min. Fourier transform infrared spectroscopy (FTIR) analysis was done by a PerkinElmer spectrum FTIR spectrometer to ratify the presence of metal−oxygen vibrational bands in MZFO nanoparticles. Scanning electron microscopy (SEM) was employed to study the microstructures of the prepared samples. The dielectric properties were examined by Wayne Kerr LCR 6500B. For dielectric and gas-sensing measurements, the homogenized powder was compressed into pellets of around ∼3 mm thickness and 13 mm diameter, at a pressure of 5 tons for 4 min.

https://doi.org/10.1021/acsomega.3c03781
ACS Omega 2023, 8, 34760−34767

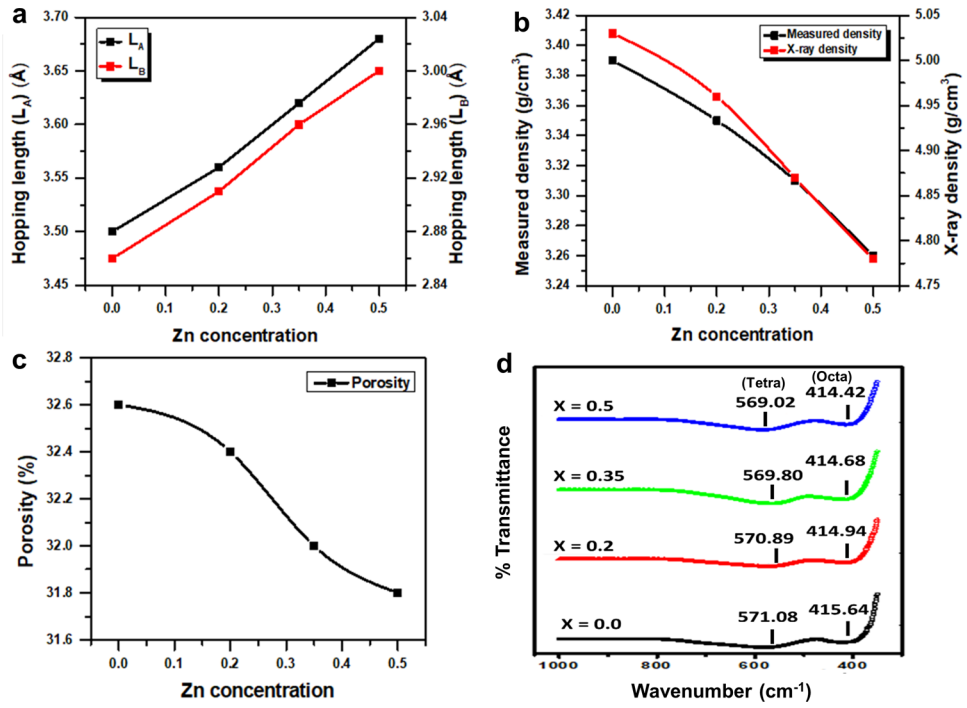

Figure 3. (a) Hopping lengths in tetrahedral sites (LA) and octahedral sites (LB) as a function of Zn-doped content, (b) measured density and X-ray density as a function of Zn-doped content, (c) porosity as a function of Zn-doped content, and (d) FTIR spectroscopy of $Mg_{1-x}Zn_xFe_2O_4$ (x = 0.0, 0.2, 0.35, and 0.5) samples.

Table 1. Structural Parameters of $Mg_{1-x}Zn_xFe_2O_4$ (x = 0.0, 0.2, 0.35, and 0.5) Samples

parameters	$MgFe_2O_4$	$Mg_{0.8}Zn_{0.2}Fe_2O_4$	$Mg_{0.65}Zn_{0.35}Fe_2O_4$	$Mg_{0.5}Zn_{0.5}Fe_2O_4$
lattice constant (α) (Å)	8.08	8.23	8.36	8.49
cell volume (V_{cell}) (α^3)	527.51	557.44	584.27	611.96
average crystallite size (D) (nm)	11.71	12.30	13.22	15.33
mass density (ρ_m) (g cm^{-3})	3.39	3.35	3.31	3.26
X-ray density (ρ_x) (g cm^{-3})	5.03	4.96	4.87	4.78
porosity (P) (%)	32.6	32.4	32	31.8
tetrahedral band position (υ_1)	571.08	570.89	569.80	569.02
octahedral band position (υ_2)	415.64	414.94	414.68	414.42
hopping lengths along tetrahedral sites (L_A)	3.50	3.56	3.62	3.68
hopping lengths along tetrahedral sites (L_B)	2.86	2.91	2.96	3.00

The sensing of various gases was done using a specially designed gas-sensing setup. The sensing system is composed of a sealed vessel with two input and output valves. The pellet sensor was mounted in the measuring chamber, and the outputs were coupled to a Keithley multimeter. The sensing response was studied using commercially available gases (CO_2, O_2, and N_2) of 99% purity. A known volume of test gas was injected into the static system through a control valve on one of the vertical walls of the closed system to achieve the required gas concentration. Sensors were connected to a constant voltage supply, and the current was measured using a digital ammeter. From the measured current, resistance was calculated as a function of time under conditions of constant temperature, both in the air and the test gas present. The experimental schematic is sketched in Figure 1.

Before the beginning of the gas testing, the sensors were heated at 100 °C for 10 min to achieve thermodynamic stabilization. For better and more reproducible results, the samples had to be heated before analysis. The sensitivity was calculated using the relationship below.[14]

$$S = \frac{\Delta R}{R_a} = \frac{|R_a - R_g|}{R_a} \quad (1)$$

where R_a and R_g represent sensor resistance in the air and test gas, respectively.

3. RESULTS AND DISCUSSION

3.1. Structural Analysis. The XRD analysis of the investigated samples is displayed in Figure 2a. The patterns showed the existence of a single-phase FCC structure. The peaks were well defined and indexed to (220), (311), (400), (422), (511), (440), (533), and (622) diffraction planes, which also show good agreement with the literature.[14−17] The high peak intensity of the (311) plane could be ascribed to an annealing process that increases the crystallinity and specific orientation of the crystallites. The lattice constants for all compositions were found to be increased from 8.08 to 8.49 Å, and average crystallite sizes using Scherer's equation[18,19] were found to be ∼13.2 nm, and it is clear from the XRD plots that the peaks shift toward lower 2θ with increasing Zn

https://doi.org/10.1021/acsomega.3c03781
ACS Omega 2023, 8, 34760−34767

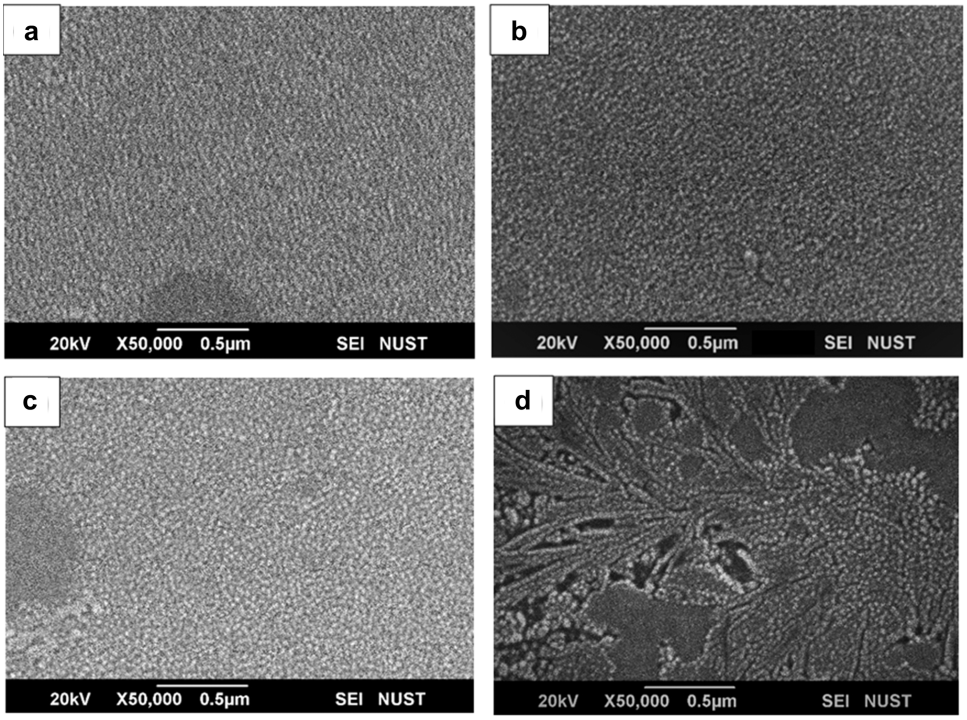

Figure 4. SEM images of $Mg_{1-x}Zn_xFe_2O_4$: (a) x = 0.0, (b) x = 0.2, (c) x = 0.35, and (d) x = 0.5 samples.

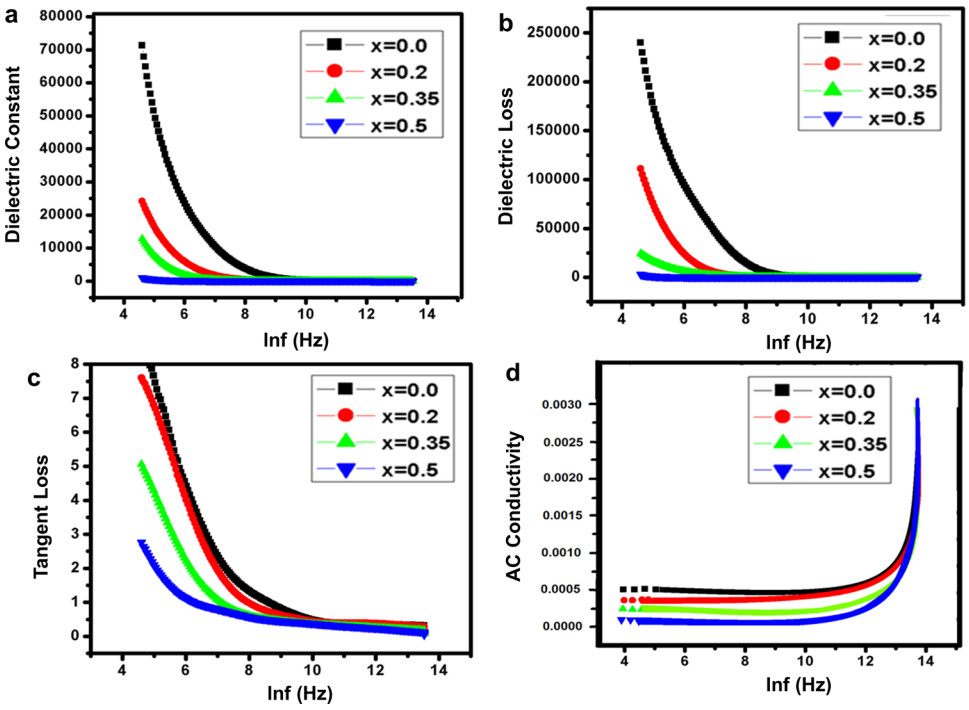

Figure 5. (a) Dielectric constant, (b) dielectric loss, (c) tangent loss, and (d) AC conductivity of $Mg_{1-x}Zn_xFe_2O_4$ (x = 0.0, 0.2, 0.35, and 0.5) samples as a function of frequency.

concentration, hence validating the increasing trends in Figure 2b.

The increase in lattice parameters with increasing Zn contents could be elucidated based on the ionic radii, where the radius of Mg is smaller than that of the Zn ion. The increase in lattice constant was further confirmed by the hopping length in tetrahedral (L_A) and octahedral sites (L_B) calculated from the reported formulas.[20] The variation in hopping lengths (L_A) and (L_B) is depicted in Figure 3a.

The hopping lengths were found to be increased with increasing zinc concentrations, which could be a result of increasing lattice constants for the samples. The measured densities (ρ_m), X-ray densities (ρ_{XRD}), and porosity were also calculated following the reported formulas.[21,22] The decrease in densities with the increase in Zn concentrations is shown in

https://doi.org/10.1021/acsomega.3c03781
ACS Omega 2023, 8, 34760−34767

Figure 3b. This can be attributed to the doping effect, where Zn^{2+} ions partially replace some of the host ions, which results in the development of neighboring, oppositely charged vacancies causing electric dipoles. The created ion vacancies could speed up the ions' interdiffusion in the solution.[23−25] This agrees with the lattice diffusion mechanism. Therefore, the general decrease in porosity is predictable, as displayed in Figure 3c. The whole structural status acquired is tabulated in Table 1.

The formation of spinel-structured pure $MgFe_2O_4$ and Zn-doped $MgFe_2O_4$ was further supported by FTIR spectra at room temperature, as presented in Figure 3d. The FTIR spectroscopy of the samples under examination showed two absorption bands, υ_1 and υ_2, because of octahedral and tetrahedral metal−oxygen bonds vibrations (see Table 1). Here, the spectra were taken in the range of 1000−300 cm^{-1}. The characteristic metal−oxygen absorption bands for the spinel ferrites at ∼414 and ∼570 cm^{-1} were seen in a given range. An absorption band's intensity is strongly affected by the synthesis process and the substituted cation. Metal and oxygen atoms at tetrahedral and octahedral sites form different bond lengths, which determine the difference between these two bands. The high-frequency band is observed in the range of 500−600 cm^{-1}, whereas the low-frequency band lies in the 390−450 cm^{-1} range. The absorption peaks shift toward low wavenumbers with the increase of Zn^{2+} concentration. This can be ascribed to the increased bond length of Fe^{3+}−O^{2-} at the tetrahedral sites, which confirms the formation of the $Mg_{1-x}Zn_xFe_2O_4$ nanostructure.[26,27]

The surface morphology of the sintered samples with different concentrations of Zn in Mg ferrites can be visualized in the SEM images shown in Figure 4a−d.

The SEM images revealed that all of the samples exhibited a compacted arrangement of homogeneous nanoparticles having a roughly spherical shape. The particle size increased from 16 to 20 nm, and consequently, the porosity, which causes an increase in the surface-to-volume ratio, decreased, resulting in a homogeneous grain size distribution with increasing doping concentration. Some agglomeration can also be witnessed as nanoparticles aggregate to achieve a lower free energy state or because of either van der Waals attraction or Brownian motion.[28]

3.2. Dielectric Behavior. Figure 5a,b shows how the dielectric constant (ε') and dielectric loss (ε'') decrease with increasing frequency until they reach a constant value for all of the samples, which can be explained by the Maxwell−Wagner[29,30] type of interfacial polarization in agreement with Koop's phenomenological theory.[31]

A mechanism analogous to the conduction process is involved in the polarization of ferrites, according to Rabinkin and Novikova.[32] In $Fe^{2+} \leftrightarrow Fe^{3+}$, the electron exchange produces a local displacement of electrons in the direction of the applied field.[33,34] These electrons are responsible for polarization. The high value of ε' at lower frequencies is because of the dominance of the species, such as Fe^{2+} ions, O_2 vacancies, grain boundaries defect, etc. The reduction in ε' with the increase in frequency is because of the species lagging during polarization in the applied field.[35] The presence of structural defects can cause electrons to accumulate in correlated states, also known as trapping centers. It thus follows that loss factor values at higher frequencies relate to the hopping of electrons. At higher frequencies, hopping of ions' ends due to prompt fluctuation of the applied field, and random orientations of dipolar moments tend to decrease the value of ε'. After a certain frequency range, the dielectric constant becomes constant for higher frequency ranges. This shows the dependency of both the dielectric constant and loss on frequencies.[36,37] The applied electric field created the dipoles; these dipole moments are well aligned because of the hopping mechanism. During the heat treatment of these samples, Fe^{2+} ions are created, making the hopping mechanism a significant factor. A relaxation of the electric field in materials occurs at higher frequencies. A lower dielectric loss factor at higher frequencies is also associated with purity in synthesized materials. In other words, good optical properties would be useful for designing many optical devices in the industry.[38,39]

The variations of tangent loss ($\tan\delta$) with frequencies have been shown in Figure 5c. All of the samples show a reduction in $\tan\delta$, which agrees with the Maxwell−Wagner model and also confirms Koop's theory.[40] If the electron hopping frequency between Fe^{2+} and Fe^{3+} equals the frequency of the applied field, $\tan\delta$ reaches its maximum value. According to this theory, electron hopping between Fe^{2+} and Fe^{3+} situated on the octahedral sites is responsible for conduction in n-type ferrites. Therefore, a maximum loss tangent can be seen when the hopping frequency is similar to the applied field. Tangent loss is a measure of how much energy has been dissipated by the material when exposed to external fields. An energy loss takes place when the phase changes at a specific frequency. In general, losses occur when the polarization of dipoles is not followed by an electric field.[41] As a result, at higher frequencies, $\tan\delta$ decreases, and at 14 MHz, it is almost zero. These characteristics allow these materials to be used for developing high-frequency devices.[42] For all synthesized samples, almost the same trend is observed.

AC conductivity may be easily determined by measuring the tangent loss factor, dielectric constant, and frequency using the relation below.[43]

$$\sigma_{ac} = 2\pi f \epsilon_0 \epsilon'' \quad (2)$$

From Figure 5d, it is evident that at lower frequencies, the AC conductivity is also low and then increases at higher frequencies. This type of behavior confirms the semiconductor nature of ferrite nanoparticles.[44] The AC trend observed in Mg−Zn ferrites nanostructures is primarily due to the relaxation and hopping mechanisms that take place among the localized states within the band gap. The mechanism of exciton hopping happens frequently at ambient temperature, resulting in a huge hopping distance.[45]

3.3. Gas-Sensing Properties. The value of sensitivity for the Mg−Zn ferrite sensors prepared by the coprecipitation technique is relatively higher because of the low crystallite size, which gives a large surface area for the test gas to be exposed. Further enhancement of the area upsurges the likelihood of gas−solid interactions and results in an increase in the sensitivity of the material.[46,47] The sensing mechanism of prepared ferrite materials is established by the property of varying the resistance of sensing materials in the presence of a determinate gas. A porous structure encourages gas molecules to penetrate the material more easily since it is reported that the pores could provide pathways for the gas to travel into the ferrite sensors and could increase the adsorption of the tested gases.[48] The porous ferrites have electrical properties that are strongly dependent on humidity.[49,50] In the present work, all of the measurements were performed at room temperature (23 °C) with a humidity level of 17%.

https://doi.org/10.1021/acsomega.3c03781
ACS Omega 2023, 8, 34760−34767

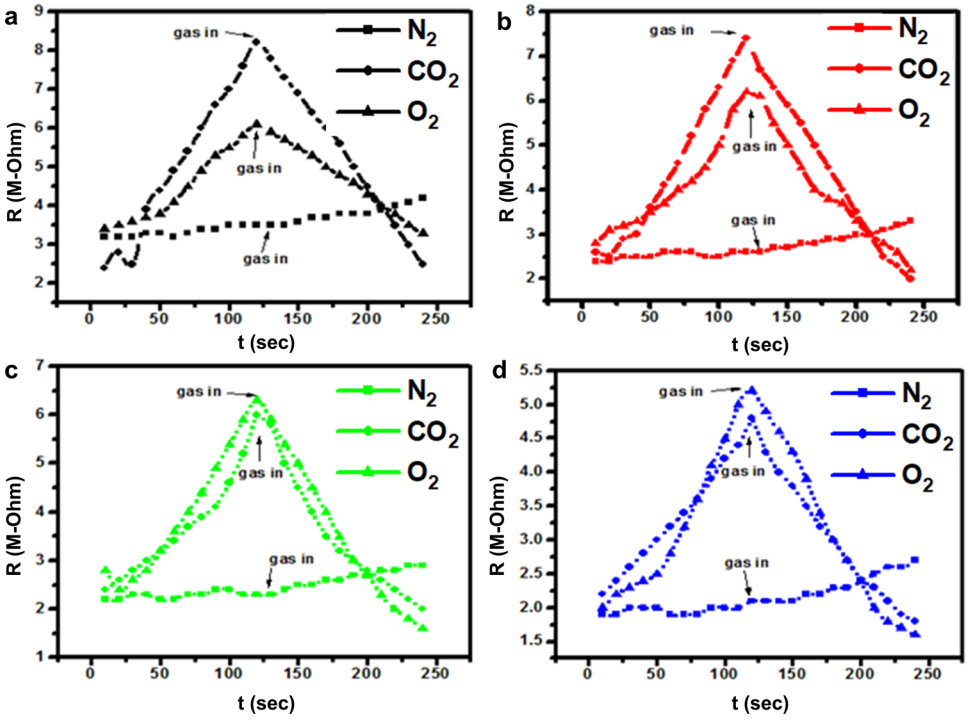

Figure 6. Resistance transient of $Mg_{1-x}Zn_xFe_2O_4$ (a) $x = 0.0$, (b) $x = 0.2$, (c) $x = 0.35$, and (d) $x = 0.5$ samples for CO_2, O_2, and N_2 gases.

The gas-sensing mechanism of ferrites is based on the surface-controlled process as follows.[51] First, oxygen absorbs the surface of the sensing material by removing electrons from the conduction band to form super-oxides or peroxides. This would result in oxygen deficiency in the bulk of the sensor, usually at the surface. Upon exposure to the gas, it reacts with the adsorbed oxygen, releasing the trapped electron into the conduction band and afterward depressing the resistance. The adsorption of the gases is affected by the kind of test gases and the sensing materials, which influence sensitivity and response time. The gas-sensing properties of various gases are due to differences in the adsorption and reaction processes. The amount of absorbed oxygen is critical for delivering sufficient reactants for the reaction to occur.

As shown in Figure 6a–d, the sensor resistance upsurges at an initial stage but declines subsequently with the time of gas exposure.

This can be elucidated qualitatively from the dynamic balance between the initial fast adsorption of exposed gas molecules and the further acceleration of desorption. Moreover, this can also be understood by considering that the reaction rate between the gas and the sensing material increases as time passes and further decreases because of the combustion of the test gas. The sensitivities of the four ferrites toward the gases CO_2, O_2, and N_2 have been compared in Figure 7 against composition, showing a decrease in sensitivities due to a decrease in the number of pores with increasing doping content.

The nanostructured samples showed exclusive sensitivity to CO_2 gas at room temperature, whereas sensitivity to other gases was comparatively low. Detailed gas-sensing parameters are tabulated in Table 2.

The sensing characteristics give an idea of the response time and are defined as the time taken by the sensor to reach 50% of the final response. It is found that MZFO exhibits a rise time (response time) of ~1 min for CO_2.

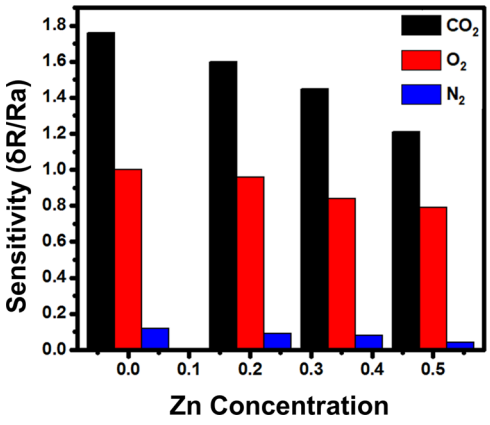

Figure 7. Sensitivity of $Mg_{1-x}Zn_xFe_2O_4$ ($x = 0.0$, 0.2, 0.35, and 0.5) samples as a function of Zn concentration among various gases.

4. CONCLUSIONS

$Mg_{1-x}Zn_xFe_2O_4$ nanoparticles were successfully synthesized by the coprecipitation technique. The XRD analysis of the samples confirmed the face-centered cubic spinel nanostructure, having lattice parameters of 8.08, 8.23, 8.36, and 8.49 Å. It was observed that both the crystallite size and the lattice parameter of nanoferrites increase with increasing Zn concentrations. The structural formation of ferrites was then confirmed by FTIR spectra, showing band ranges of 500–600 cm^{-1} for tetrahedral and 390–450 cm^{-1} for octahedral lattice sites. The dielectric study showed a very low dielectric loss of Zn-doped magnesium ferrites at frequencies over 10 MHz. The sample with the composition $x = 0.5$ not only possesses a uniformly low dielectric constant at all frequencies but also exhibits a low loss factor. These are important properties in the majority of electronics; such devices can effectively function over a wide frequency range. $Mg_{1-x}Zn_xFe_2O_4$ nanoparticles were found to be more sensitive to CO_2 than O_2 and N_2. The

https://doi.org/10.1021/acsomega.3c03781
ACS Omega 2023, 8, 34760–34767

Table 2. Gas-Sensing Characteristics (Sensitivity, Response Time) of $Mg_{1-x}Zn_xFe_2O_4$ (x = 0.0, 0.2, 0.35, and 0.5) Samples

	CO_2		O_2		N_2	
samples	sensitivity	response time (s)	sensitivity	response time (s)	sensitivity	response time (s)
$MgFe_2O_4$	1.76	∼65	1	∼75	0.12	∼120
$Mg_{0.8}Zn_{0.2}Fe_2O_4$	1.60	∼66	0.96	∼77	0.09	∼122
$Mg_{0.65}Zn_{0.35}Fe_2O_4$	1.48	∼69	0.87	∼79	0.08	∼126
$Mg_{0.5}Zn_{0.5}Fe_2O_4$	1.21	∼70	0.79	∼80	0.04	∼130

preliminary results have shown that the effects of Zn ions in Mg ferrite on gas sensitivity can be related to porosity. The sensor showed a good response of ∼1 min to CO_2 gas. It was observed that the gas sensitivity depends on the types of semiconducting materials, the concentration of dopants, and the test gases to be detected and concluded that ferrite materials have useful properties and potential applications in the fields of health, industry, and agriculture.

AUTHOR INFORMATION

Corresponding Author

Farhan Javaid − *Department of Materials Engineering (ME), School of Chemical and Materials Engineering (SCME), National University of Sciences and Technology (NUST), Islamabad 44000, Pakistan;* orcid.org/0000-0003-0664-0570; Phone: +92-51-9085-5218; Email: farhan.javaid@scme.nust.edu.pk; Fax: +92-51-9085-5002

Authors

Iqra Nazir − *School of Natural Sciences (SNS), National University of Sciences and Technology (NUST), Islamabad 44000, Pakistan*

Mutawara Mahmood Baig − *Department of Materials Engineering (ME), School of Chemical and Materials Engineering (SCME), National University of Sciences and Technology (NUST), Islamabad 44000, Pakistan*

Muhammad Shoaib Butt − *Department of Materials Engineering (ME), School of Chemical and Materials Engineering (SCME), National University of Sciences and Technology (NUST), Islamabad 44000, Pakistan;* orcid.org/0000-0002-7689-339X

Iftikhar Hussain Gul − *Department of Materials Engineering (ME), School of Chemical and Materials Engineering (SCME), National University of Sciences and Technology (NUST), Islamabad 44000, Pakistan*

Complete contact information is available at: https://pubs.acs.org/10.1021/acsomega.3c03781

Author Contributions

I.N. contributed to conceptualization, methodology, formal analysis, investigation, and writing the original draft. F.J. contributed to conceptualization, methodology, investigation and writing, review, editing, and validation. M.M.B. contributed to conceptualization, formal analysis, investigation, writing, review, and editing. M.S.B. contributed to review, editing, and validation. I.H.G. contributed to conceptualization, methodology, formal analysis, writing, review, editing, visualization, and supervision. All authors have read and agreed to the published version of the manuscript.

Notes

The authors declare no competing financial interest.

REFERENCES

(1) Jahan, N.; Khan, M. N. I.; Khandaker, J. I. Exploration through Structural, Electrical, and Magnetic Properties of Al3+Doped Ni-Zn-Co Nanospinel Ferrites. *ACS Omega* **2021**, *6*, 32852−32862.

(2) Vinosha, P. A.; Manikandan, A.; Judith Ceicilia, A. S.; et al. Review on recent advances of zinc substituted cobalt ferrite nanoparticles: Synthesis characterization and diverse applications. *Ceram. Int.* **2021**, *47*, 10512−10535.

(3) Chen, D.; Luo, F.; Gao, L.; Zhou, W.; Zhu, D. Dielectric and microwave absorption properties of divalent-doped Na3Zr2Si2PO12 ceramics. *J. Eur. Ceram. Soc.* **2018**, *38*, 4440−4445.

(4) Srinivasamurthy, K. M.; Manjunatha, K.; El-Denglawey, A.; et al. Evaluation of structural, dielectric and LPG gas sensing behavior of porous Ce3+- Sm3+ doped Cobalt nickel ferrite. *Mater. Chem. Phys.* **2022**, *275*, No. 125222.

(5) Kefeni, K. K.; Msagati, T. A. M.; Nkambule, T. T.; Mamba, B. B. Spinel ferrite nanoparticles and nanocomposites for biomedical applications and their toxicity. *Mater. Sci. Eng. C* **2020**, *107*, No. 110314.

(6) Jana, R.; Hajra, S.; Rajaitha, P. M.; Mistewicz, K.; Kim, H. J. Recent advances in multifunctional materials for gas sensing applications. *J. Environ. Chem. Eng.* **2022**, *10*, No. 108543.

(7) Yang, H.; Bai, X.; Hao, P.; et al. A simple gas sensor based on zinc ferrite hollow spheres: Highly sensitivity, excellent selectivity and long-term stability. *Sens. Actuators, B* **2019**, *280*, 34−40.

(8) Narang, S. B.; Pubby, K. Nickel Spinel Ferrites: A review. *J. Magn. Magn. Mater.* **2021**, *519*, No. 167163.

(9) Ali, A.; Gul, I. H.; Khan, M. Z.; Javaid, F. Improved photocatalytic degradation efficiency of methylene blue via MgAl2O4−graphene nanocomposite. *J. Korean Ceram. Soc.* **2022**, *60*, 293−300.

(10) Kuru, T. Ş.; Kuru, M.; Bağcı, S. Structural, dielectric and humidity properties of Al-Ni-Zn ferrite prepared by co-precipitation method. *J. Alloys Compd.* **2018**, *753*, 483−490.

(11) Murugesan, C.; Ugendar, K.; Okrasa, L.; Shen, J.; Chandrasekaran, G. Zinc substitution effect on the structural, spectroscopic and electrical properties of nanocrystalline MnFe2O4 spinel ferrite. *Ceram. Int.* **2021**, *47*, 1672−1685.

(12) Wu, K.; Li, J.; Zhang, C. Zinc ferrite based gas sensors: A review. *Ceram. Int.* **2019**, *45*, 11143−11157.

(13) Hankare, P. P.; Jadhav, S. D.; Sankpal, U. B.; Patil, R. P.; Sasikala, R.; Mulla, I. S. Gas sensing properties of magnesium ferrite prepared by co-precipitation method. *J. Alloys Compd.* **2009**, *488*, 270−272.

(14) Bharti, D. C.; Mukherjee, K.; Majumder, S. B. Wet chemical synthesis and gas sensing properties of magnesium zinc ferrite nanoparticles. *Mater. Chem. Phys.* **2010**, *120*, 509−517.

(15) Păcurariu, C.; Lazău, I.; Ecsedi, Z.; Lazău, R.; Barvinschi, P.; Mărginean, G. New synthesis methods of MgAl2O4 spinel. *J. Eur. Ceram. Soc.* **2007**, *27*, 707−710.

(16) Saberi, A.; Golestani-Fard, F.; Sarpoolaky, H.; Willert-Porada, M.; Gerdes, T.; Simon, R. Chemical synthesis of nanocrystalline magnesium aluminate spinel via nitrate-citrate combustion route. *J. Alloys Compd.* **2008**, *462*, 142−146.

(17) Kutty, P. V. M.; Dasgupta, S. Low temperature synthesis of nanocrystalline magnesium aluminate spinel by a soft chemical method. *Ceram. Int.* **2013**, *39*, 7891−7894.

(18) Khan, M. Z.; Gul, I. H.; Baig, M. M.; Khan, A. N. Comprehensive study on structural, electrical, magnetic and photo-

https://doi.org/10.1021/acsomega.3c03781
ACS Omega 2023, 8, 34760−34767

catalytic degradation properties of Al3+ ions substituted nickel ferrites nanoparticles. *J. Alloys Compd.* **2020**, *848*, No. 155795.
(19) Ahmad, R.; Iqbal, N.; Baig, M. M.; Noor, T.; Ali, G.; Gul, I. H. ZIF-67 derived nitrogen doped CNTs decorated with sulfur and Ni(OH)2 as potential electrode material for high-performance supercapacitors. *Electrochim. Acta* **2020**, *364*, No. 137147.
(20) Patil, V. G.; Shirsath, S. E.; More, S. D.; Shukla, S. J.; Jadhav, K. M. Effect of zinc substitution on structural and elastic properties of cobalt ferrite. *J. Alloys Compd.* **2009**, *488*, 199−203.
(21) Kaur, N.; Kaur, M. Comparative studies on impact of synthesis methods on structural and magnetic properties of magnesium ferrite nanoparticles. *Process. Appl. Ceram.* **2014**, *8*, 137−143.
(22) Iqbal, M. J.; Farooq, S. Effect of doping of divalent and trivalent metal ions on the structural and electrical properties of magnesium aluminate. *Mater. Sci. Eng. B* **2007**, *136*, 140−147.
(23) Malik, S.; Gul, I. H.; Baig, M. M. Hierarchical MnNiCo ternary metal oxide/graphene nanoplatelets composites as high rated electrode material for supercapacitors. *Ceram. Int.* **2021**, *47*, 17008−17014.
(24) Baig, M. M.; Gul, I. H. Transformation of wheat husk to 3D activated carbon/NiCo2S4 frameworks for high-rate asymmetrical supercapacitors. *J. Energy Storage* **2021**, *37*, No. 102477.
(25) Elizbit; Liaqat, U.; Hussain, Z.; Baig, M. M.; Khan, M. A.; Arif, D. Preparation of porous ZIF-67 network interconnected by MWCNTs and decorated with Ag nanoparticles for improved non-enzymatic electrochemical glucose sensing. *J. Korean Ceram. Soc.* **2021**, *58*, 598−605.
(26) Khan, M. A.; Mehran, M. T.; Naqvi, S. R.; et al. Reutilizing Methane Reforming Spent Catalysts as Efficient Overall Water-Splitting Electrocatalysts. *ACS Omega* **2021**, *6*, 21316−21326.
(27) Khan, R.; Mehran, M. T.; Naqvi, S. R.; et al. A highly efficient A-site deficient perovskite interlaced within two dimensional MXene nanosheets as an active electrocatalyst for hydrogen production. *Int. J. Hydrogen Energy* **2022**, *47*, 37476−37489.
(28) Banfield, J. F.; Welch, S. A.; Zhang, H.; Ebert, T. T.; Penn, R. L. Aggregation-Based Crystal Growth and Microstructure Development in Natural Iron Oxyhydroxide Biomineralization Products. *Science* **2000**, *289*, 751−754.
(29) Johnstone, J. H. L.; Williams, J. W. The Variation of Dielectric Constant with Frequency. *Phys. Rev.* **1929**, *34*, 1483−1490.
(30) Gabal, M. A.; Al-Juaid, A. A. Structural and electromagnetic studies of Mg1-xZnxFe2O4 nanoparticles synthesized via a sucrose autocombustion route. *J. Mater. Sci. Mater. Electron.* **2020**, *31*, 10055−10071.
(31) Koops, C. G. On the Dispersion of Resistivity and Dielectric Constant of Some Semiconductors at Audiofrequencies. *Phys. Rev.* **1951**, *83*, 121−124.
(32) Gul, I. H.; Abbasi, A. Z.; Amin, F.; Anis-ur-Rehman, M.; Maqsood, A. Structural, magnetic and electrical properties of Co1−xZnxFe2O4 synthesized by co-precipitation method. *J. Magn. Magn. Mater.* **2007**, *311*, 494−499.
(33) Araújo, J.; Araujo-Barbosa, S.; Souza, A. L. R.; et al. Tuning structural, magnetic, electrical, and dielectric properties of MgFe2O4 synthesized by sol-gel followed by heat treatment. *J. Phys. Chem. Solids* **2021**, *154*, No. 110051.
(34) Hirthna; Sendhilnathan, S. Enhancement in dielectric and magnetic properties of Mg2+ substituted highly porous super paramagnetic nickel ferrite nanoparticles with Williamson-Hall plots mechanistic view. *Ceram. Int.* **2017**, *43*, 15447−15453.
(35) Akhtar, M. S.; Gul, I. H.; Baig, M. M.; Akram, M. A. Binder-free pseudocapacitive nickel cobalt sulfide/MWCNTs hybrid electrode directly grown on nickel foam for high rate supercapacitors. *Mater. Sci. Eng. B* **2021**, *264*, No. 114898.
(36) Azad, M.; Hussain, Z.; Baig, M. M. MWCNTs/NiS2 decorated Ni foam based electrode for high-performance supercapacitors. *Electrochim. Acta* **2020**, *345*, No. 136196.
(37) Baig, M. M.; Gul, I. H.; Khan, M. Z.; Mehran, M. T.; Akhtar, M. S. Binder-free heterostructured MWCNTs/Al2S3 decorated on NiCo foam as highly reversible cathode material for high-performance supercapacitors. *Electrochim. Acta* **2020**, *340*, No. 135955.
(38) Khan, R.; Mehran, M. T.; Baig, M. M.; et al. 3D hierarchical heterostructured LSTN@NiMn-layered double hydroxide as a bifunctional water splitting electrocatalyst for hydrogen production. *Fuel* **2021**, *285*, No. 119174.
(39) Baig, M. M.; Pervaiz, E.; Azad, M.; Jahan, Z.; Khan Niazi, M. B.; Baig, S. M. NiFe2O4/SiO2 nanostructures as a potential electrode material for high rated supercapacitors. *Ceram. Int.* **2021**, *47*, 12557−12566.
(40) Omri, A.; Dhahri, E.; Costa, B. F. O.; Valente, M. A. Structural, electric and dielectric properties of Ni0.5Zn0.5FeCoO4 ferrite prepared by sol-gel. *J. Magn. Magn. Mater.* **2020**, *499*, No. 166243.
(41) Deonikar, V. G.; Kulkarni, V. D.; Rathod, S. M.; Kim, H. Fabrication and characterizations of structurally engineered lanthanum substituted nickel-cobalt ferrites for the analysis of electric and dielectric properties. *Inorg. Chem. Commun.* **2020**, *119*, No. 108074.
(42) Mahalakshmi, S.; Jayasri, R.; Nithiyanatham, S.; Swetha, S.; Santhi, K. Magnetic interactions and dielectric behaviour of cobalt ferrite and barium titanate multiferroics nanocomposites. *Appl. Surf. Sci.* **2019**, *494*, 51−56.
(43) Ahmad, S. I.; Rauf, A.; Mohammed, T.; Bahafi, A.; Ravi Kumar, D.; Suresh, M. B. Dielectric, impedance, AC conductivity and low-temperature magnetic studies of Ce and Sm co-substituted nanocrystalline cobalt ferrite. *J. Magn. Magn. Mater.* **2019**, *492*, No. 165666.
(44) Murugesan, C.; Okrasa, L.; Chandrasekaran, G. Structural, AC conductivity, impedance and dielectric study of nanocrystalline MFe2O4 (M = Mg, Co or Cu) spinel ferrites. *J. Mater. Sci. Mater. Electron.* **2017**, *28*, 13168−13175.
(45) Al-Bassami, N. S.; Mansour, S. F. AC conductivity, complex impedance and photocatalytic applications of Co2+ substituted Mg−Zn nanoferrite. *Appl. Phys. A* **2021**, *127*, 38.
(46) Durga Prasad, P.; Hemalatha, J. Enhanced magnetic properties of highly crystalline cobalt ferrite fibers and their application as gas sensors. *J. Magn. Magn. Mater.* **2019**, *484*, 225−233.
(47) Zhang, P.; Qin, H.; Lv, W.; Zhang, H.; Hu, J. Gas sensors based on ytterbium ferrites nanocrystalline powders for detecting acetone with low concentrations. *Sens. Actuators, B* **2017**, *246*, 9−19.
(48) Abu-Hani, A. F. S.; Mahmoud, S. T.; Awwad, F.; Ayesh, A. I. Design, fabrication, and characterization of portable gas sensors based on spinel ferrite nanoparticles embedded in organic membranes. *Sens. Actuators, B* **2017**, *241*, 1179−1187.
(49) Manikandan, V.; Petrila, I.; Vigneselvan, S.; et al. Efficient humidity-sensitive electrical response of annealed lithium substituted nickel ferrite (Li−NiFe2O4) nanoparticles under ideal, real and corrosive environments. *J. Mater. Sci. Mater. Electron.* **2018**, *29*, 18660−18667.
(50) Manikandan, V.; Petrila, I.; Kavita, S.; et al. Effect of Vd-doping on dielectric, magnetic and gas sensing properties of nickel ferrite nanoparticles. *J. Mater. Sci. Mater. Electron.* **2020**, *31*, 16728−16736.
(51) Waghmare, S. D.; Raut, S. D.; Ghule, B. G.; et al. Pristine and palladium-doped perovskite bismuth ferrites and their nitrogen dioxide gas sensor studies. *J. King Saud Univ. − Sci.* **2020**, *32*, 3125−3130.

https://doi.org/10.1021/acsomega.3c03781
ACS Omega 2023, 8, 34760−34767